

University of South Dakota

USD RED

Dissertations and Theses

Theses, Dissertations, and Student Projects

2022

CHARACTERIZATION OF UNDOPED CSI AT CRYOGENIC TEMPERATURES

Yongjin Yang

Follow this and additional works at: <https://red.library.usd.edu/diss-thesis>



Part of the [Physics Commons](#)

CHARACTERIZATION OF UNDOPED CSI AT CRYOGENIC TEMPERATURES

By

Yongjin Yang

B.S., North China University of Science and Technology, 2015


A Thesis Submitted in Partial Fulfillment of
the Requirements for the Degree of
Master of Physics

Department of Physics

Analytics for Large Data Sets Program
In the Graduate School
The University of South Dakota
August 2022

The members of the Committee appointed to examine the
thesis/dissertation of Yongjin Yang find it satisfactory
and recommend that it be accepted.

DocuSigned by:



D7C37880D26F476...

Chairperson, Jing Liu

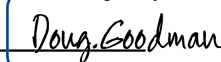
DocuSigned by:



3A24A6D89824AD...

Dongming Mei

DocuSigned by:



1AF176046C6E4D6...

Doug Goodman

ABSTRACT

Doped CSI (Cesium iodide) is widely used in many detectors. Pure cesium iodide can only perform well at low temperature due to its luminous properties. Its luminous efficiency at low temperature is even better than that of impurity-containing cesium iodide. So we want to measure its properties at low temperatures.

In chapter 1, we have the information about the neutrino and scintillator detectors background. We also introduce some scintillator detectors which is using in the COHERENT.

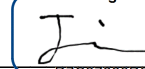
In chapter 2, our focus is on scintillator detectors and the pure CsI crystal.

In chapter 3, we measure the light yield of the pure CSI, which is the important property as a detector. We also introduce our experimental equipment and methods.

In chapter 4, the quenching factor represents the efficiency of energy deposition. This value is a key point for our future detection of neutrinos.

Thesis Advisor

DocuSigned by:



D7C37880D26F476...

Jing Liu

Contents

Committee signature page	i
ABSTRACT	ii
List of Tables	iv
List of Figures	v
1. Introduction	1
1.1 Neutrino	1
1.2 Testing non-standard interactions with CevNS	4
1.3 COHERENT detector in Neutrino Alley	6
2. Scintillator Detectors	9
3.1 What is Scintillators?	9
3.2 Scintillation Mechanism	10
3.3 CsI Crystal	11
3. Light Yield Measurement	13
3.1 Our cryostat.....	13
3.2 Data format	16
3.3 Single PE Measurement.....	19
3.4 Light Yield Measurement	22
4. Quenching Factor Measurement.....	25
4.1 Quenching factor.....	25
4.2 Simulation	26
4.3 Time of Flight Measurement.....	29
4.4 Light Yield Measurement with PMT	30
4.5 Quenching Factor Measurement.....	32
5. Conclusion	35
References	36

List of Tables

Table 1 Parameters of subsystems for CEvNS detection. (Highlight means they have been planed to use in future)	7
Table 2 Additional detectors that broaden the physics reach of COHERENT.(Highlight means they have been planed to use in future)	7
Table 3 Fitting results of ^{241}Am peaks in energy spectra.....	22
Table 4 Neutron events time of flight at different distance	30

List of Figures

Figure 1 Sketch of CEvNS interaction (left) and its corresponding Feynman diagram (right).	1
Figure 2 Neutrino cross sections for neutrino energies up to 55 MeV relevant for COHERENT	2
Figure 3 Figures of merit for stopped-pion neutrino sources worldwide (past, current and future).	3
Figure 4 Distributions of neutrino energy (left) and creation time (right) produced at the SNS predicted by our Geant4 simulation ⁴	4
Figure 5 Current and near-future detector subsystems in Neutrino alley.	6
Figure 6 Scintillation Mechanism Principle	10
Figure 7 Light yield for different crystal in different temperature	12
Figure 8 Cryostat design diagram (Left) and the experiment setup in our lab (Right)	13
Figure 9 The circuit diagram of PMT	14
Figure 10 Cryostat inside setup (left) and the IR Shield (right).	15
Figure 11 Single PE waveform (left) and the multiple PEs waveform (right)	19
Figure 12 Single PE response fitting from Pedestal to three PEs	20
Figure 13 A randomly selected light pulse within the 59.5 keV peak from the PMT.	21
Figure 14 Light Yield Measurement with Am241 and Fe55 x-axis is the area of the events after intergration	23
Figure 15 5.9KeV(left) and 59.5KeV(right) overshooting correct	23
Figure 16 Simulation back detectors setup(left) and back detectors setup(right)	27
Figure 17 Energy deposit in crystal triggered on 32.3 degree back detector.	28

Figure 18 Time of flight measurement setup priciple.....	29
Figure 19 Time of flight of 3.5m neutron events(left) and neutron and gamma events concentration.....	30
Figure 20 Experiment Setup (Left figure is the whole experiment setup. The vacuum machine is on the right. The right figure shows the hardwares.)	31
Figure 21 Light yeild(blue) and SPE(orange) measurement over time(every 2 hours during the QF measurement)the unit of x-axis is 2 hours between each other.....	32
Figure 22 Top view of the experiment setup (left) and Front view of experiment setup (right).	32
Figure 23 Quenching Factor Measurement principle.	33
Figure 24 Energy deposit in the crystal triggered on 45 degree back detector	33

1. Introduction

Doped CsI (Cesium iodide) and NaI(Sodium iodide) are widely used as detectors to detect the neutrinos event. ^{185}Kg NaI[Tl] has been used as detector in COHERENT. But pure CsI can only perform well at low temperature due to its scintillator mechanism. The light yield at low temperature is even better than that of doped CsI and NaI. So, we want to study its characterization at low temperature.

1.1 Neutrino

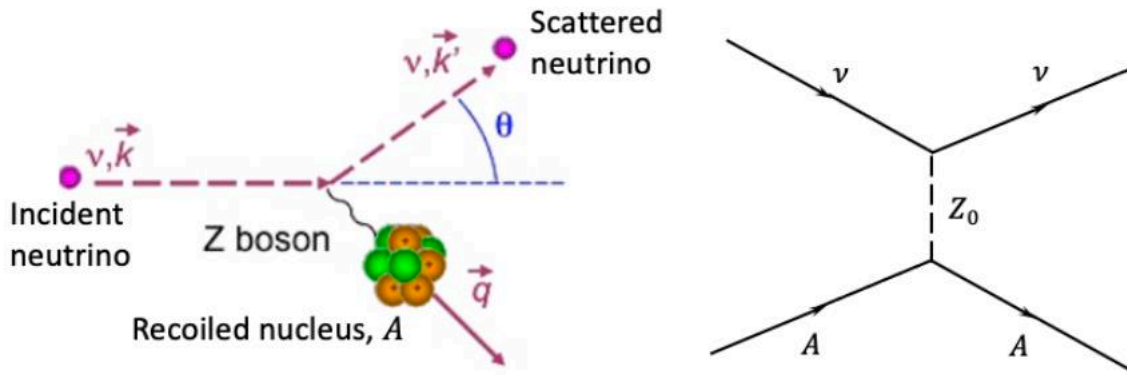


Figure 1 Sketch of CEvNS interaction (left) and its corresponding Feynman diagram (right).

Coherent elastic neutrino-nucleus scattering (CEvNS) is a weak neutral-current process in a low-energy neutrino. The coherence condition, in which the neutrino scatters off all nucleons of the nucleus in phase with each other, is satisfied when the neutrino energy is in the tens of MeV range and its momentum transfer to the recoiling nucleus is small (sub keV to keV range). As a neutrino interacts with a nucleus as a whole, the CEvNS cross section is much larger than those of charged-current (CC) neutrino interactions, where a neutrino interacts with an individual electron or quark, which is shown clearly in Figure 1.

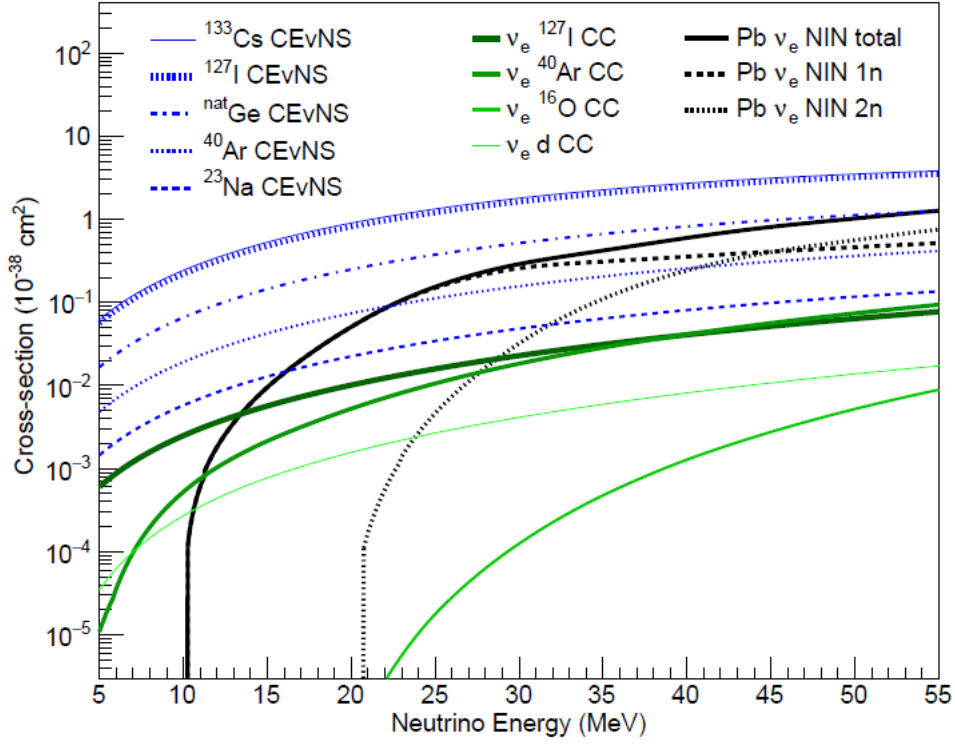


Figure 2 Neutrino cross sections for neutrino energies up to 55 MeV relevant for COHERENT

The differential cross section of CEvNS predicted by the Standard Model reads² :

$$\frac{d\sigma}{dT}(T, E_\nu) = \frac{G_F^2 M}{2\pi} \left[(G_V + G_A)^2 + (G_V - G_A)^2 \left(1 - \frac{T}{E_\nu}\right)^2 - (G_V^2 - G_A^2) \frac{MT}{E_\nu^2} \right]$$

where T is the recoil energy, E_ν is the incident neutrino energy, G_F is the Fermi constant, M is the target nuclear mass,

$$G_V = (g_V^p Z + g_V^n N) F_{nucl}^V(Q^2)$$

$$G_A = (g_A^p (Z_+ - Z_-) + g_A^n (N_+ - N_-)) F_{nucl}^A(Q^2)$$

$g_V^{n,p}$ and $g_A^{n,p}$ are vector and axial-vector coupling factors, respectively, for protons and neutrons, Z and N are the proton and neutron numbers, Z_\pm and N_\pm refer to the number of spin up or down nucleons, $F_{nucl}^{V,A}$ are vector and axial nuclear form factors, and Q is the momentum

transfer. As the numbers of spin up and down nucleons in a nucleus are either precisely or much smaller than the number of nucleons, the axial-vector contribution G_A is small. The couplings are subject to percent-level Q-dependent radiative corrections³, with values of $g_V^n \sim -0.511$ and $g_V^p \sim 0.03$.

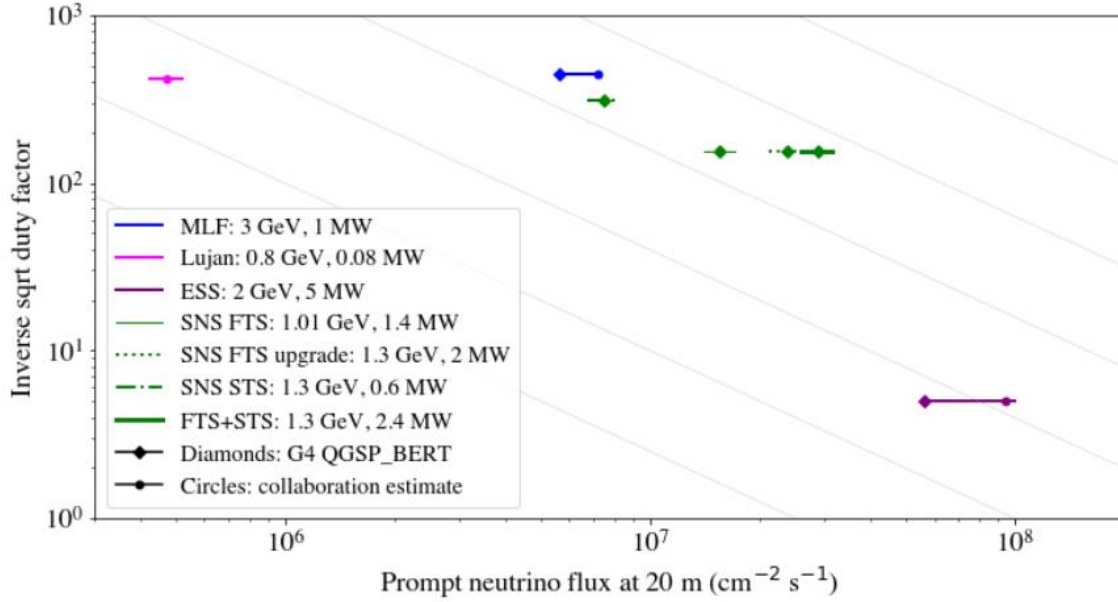


Figure 3 Figures of merit for stopped-pion neutrino sources worldwide (past, current and future). The x-axis shows ν_μ flux. This plot demonstrates the impact of sharp pulsing on flavor separation. The y-axis here represents the duty factor computed using the time window that can be used for prompt ν_μ selection.

The x-axis shows ν_μ flux. This plot demonstrates the impact of sharp pulsing on flavor separation. The y-axis here represents the duty factor computed using the time window that can be used for prompt ν_μ selection. For the MLF, for which there are two pulses separated by 540

ns, only the first one is considered. This plot considers only current and near-future sources.

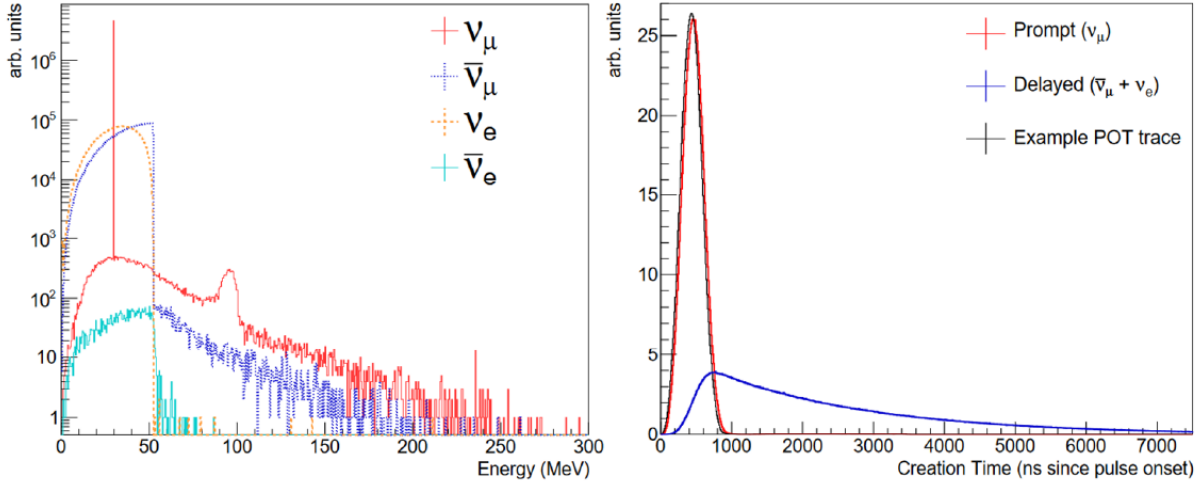


Figure 4 Distributions of neutrino energy (left) and creation time (right) produced at the SNS predicted by our Geant4 simulation⁴

1.2 Testing non-standard interactions with CEvNS

Non-standard interactions (NSI) between neutrinos and quarks would modify the CEvNS cross section. Such interactions are generally described by a matrix of vector couplings, $\epsilon_{\alpha\beta}^q$,² with a Lagrangian:

$$\mathcal{L} = \sum_{q,\alpha,\beta} 2\sqrt{2} G_F \epsilon_{\alpha\beta}^q (\bar{\nu}_\alpha \gamma^\mu (1 - \gamma^5) \nu_\beta) (\bar{q} \gamma_\mu (1 - \gamma^5) q),$$

assuming the mediator of these new interactions is heavy, $\sqrt{Q^2} = \sqrt{2m_N E_r} = 50$ MeV. The terms ϵ_{ee}^q , $\epsilon_{\mu\mu}^q$, and $\epsilon_{\tau\tau}^q$ interfere with standard-model CEvNS and break lepton universality predicted for CEvNS at tree level while $\epsilon_{e\mu}^q$, $\epsilon_{e\tau}^q$, and $\epsilon_{\mu\tau}^q$ allow for flavor-changing transitions. Non-zero values of $\epsilon_{\alpha\beta}^q$ would change the CEvNS cross section by modifying the weak charge,

$$Q_\alpha^2 = [Z(g_p^V + 2\varepsilon_{\alpha\alpha}^u + \varepsilon_{\alpha\alpha}^d) + N(g_n^V + \varepsilon_{\alpha\alpha}^u + 2\varepsilon_{\alpha\alpha}^d)]^2 + \sum_{\alpha \neq \beta} [Z(2\varepsilon_{\alpha\beta}^u + \varepsilon_{\alpha\beta}^d) + N(\varepsilon_{\alpha\beta}^u + 2\varepsilon_{\alpha\beta}^d)]^2.$$

Development of precise CEvNS measurements by COHERENT offers a novel strategy for constraining these effective parameters, many of which were previously only constrained to \sim unity. Understanding these parameters is critical for proper interpretation of neutrino oscillation data since various choices of $\varepsilon_{\alpha\beta}^q$ can bias experimental determination of neutrino mixing parameters such as Δm_{32}^2 ⁶, δ_{CP} ⁷, and θ_{12} ⁸.

As NSI parameters will generally make the CEvNS cross section different for different flavors of neutrino, a source with multiple flavors is ideal. The SNS offers a prompt ν_μ flux separated in time from delayed $\bar{\nu}_\mu/\nu_e$ allowing us to test the flavored CEvNS cross sections, $\langle\sigma\rangle_\mu$ and $\langle\sigma\rangle_e$ as described in ⁹. A deviation of $\langle\sigma\rangle_\mu/\langle\sigma\rangle_e$ from the standard model expectation would be a sensitive probe of BSM physics, including NSI, as most systematic uncertainties in the ratio correlate. The sensitivity of future COHERENT detectors to measuring these quantities is shown in . compared to the measurement based on the full CsI[Na] dataset⁹. Large CEvNS detectors will significantly improve on our current understanding of the flavored cross sections which will subsequently reduce viable NSI parameter space.

There are several measurements at 77K with α -particles which shows 85 percent to 100 percent quenching factor in pure CsI crystals. But in a recent study, it was observed that the quenching factor of alpha particles varied with crystal temperature. Around 77 K, the quench factor is even greater than one. However, the quench factor reported in another measurement at 108 K is very similar to that of CsI[Na] at room temperature. Possible causes of the discrepancy include different recoiled nuclei (Cs or I versus α), measurement temperatures or origins of

crystals. A series of measurements at the Triangle Universities Nuclear Laboratory (TUNL) will be performed by COHERENT collaborators to verify the quenching factor of CsI down to 40 K. To be conservative, a quenching factor¹⁰ of 5% is assumed in sensitivity calculations.

1.3 COHERENT detector in Neutrino Alley

The COHERENT Collaboration has deployed and is developing a number of subsystems with diverse target nuclei and detector technologies for the detection of neutrinos, neutrons, and possibly, dark matter particles from the SNS, as listed in **Error! Reference source not found.** and **Error! Reference source not found.**. They are located 19 - 28 meters from the Hg target in the basement of the SNS in what is known colloquially as Neutrino Alley, as shown in Figure 5.

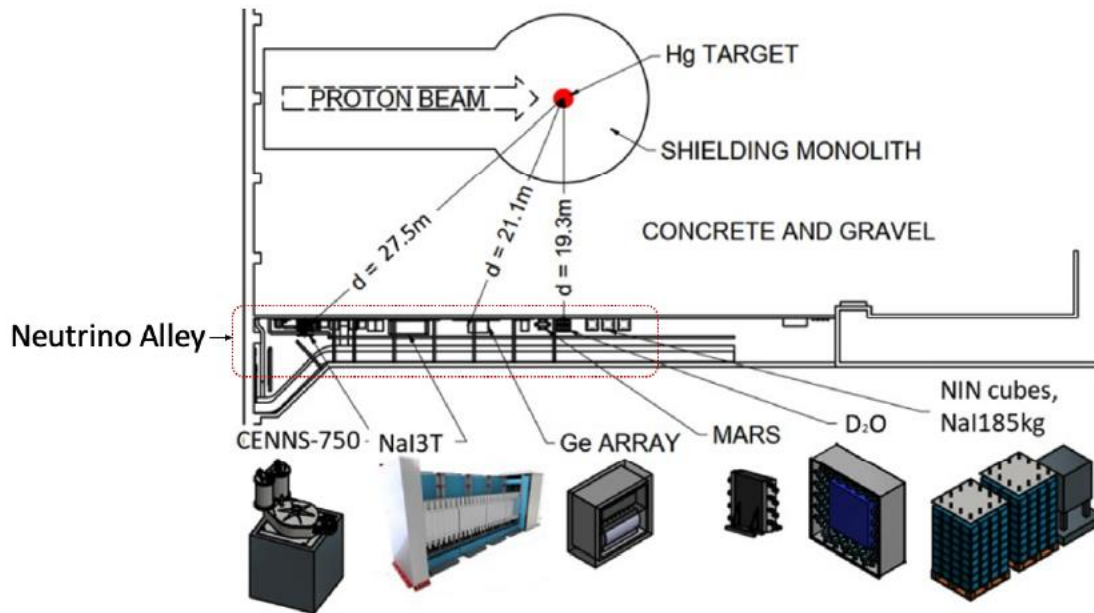


Figure 5 Current and near-future detector subsystems in Neutrino alley.

With a 1 GeV proton beam, simulations⁵ predict a flux of 4.7×10^7 neutrinos/cm² 20 m away from the target. Despite the proximity to the SNS beamline, beam-related neutrons are

suppressed by a concrete fill between Neutrino Alley and the SNS target. Cosmogenic

Table 1 Parameters of subsystems for CEvNS detection. (Highlight means they have been planned to use in future)

Nuclear target	Detector Technology	Target Mass (kg)	Distance from source	Energy thresh- old (keV [†])	Deployment dates
CsI[Na]	Scintillating crystal	14	20 m	5.4	2015-2019
Ar	Single-phase LAr★	24	29 m	20	2016-2021
Ge	HPGe PPC [‡]	18	22 m	5	2022
NaI[Tl]	Scintillating Crystal	3500	22 m	13	2022
Ar	Single-phase LAr★	750	29 m	20	2025
Ge	HPGe PPC [‡]	50	22 m	5	2025
CsI	CsI+SiPM arrays at 40 K	10~15	20 m	1.4	2025

Finished Planned, ★liquid argon, [‡]p-type point-contact, [†]nuclear recoil energy

background is reduced by an 8 m.w.e. (meter water equivalent) overburden. Due to the relatively large cross section of the CEvNS interaction for heavy nuclei and an intense neutrino source with excellent background rejection, detector mass can be reduced from the multiple kiloton range down to the kilogram scale.

The collaboration is adopting a more systematic naming scheme for its various subsystems, which starts with ``COH-'', followed by the target material, ``-Ge'' for example, and phase number, ``-2'', for example. The 50kg HPGe subsystem listed in **Error! Reference source not found.** in this new naming scheme is called ``COH-Ge-2'', and the 10kg CsI operated at 40K is called ``COH-CryoCsI-1''. For historical reasons, the 750kg liquid argon detector is called

Table 2 Additional detectors that broaden the physics reach of COHERENT.(Highlight means they have been planned to use in future)

Name	Detector Technology	Main purpose	Deployment dates
NaIVE	185 kg NaI[Tl] crystals	Measure $\nu_e + \text{I CC}^\ddagger$ cross section & beam-related backgrounds	2016 - present
MARS	scintillation panels interleaved with Gd-painted foils	measure beam-related neutrons in Neutrino Alley	2017 - present
NIN cubes	liquid scintillator cells in lead and iron shields	measure neutrino-induced neutrons (NIN) in lead & iron	2019 - present
D ₂ O	heavy water Cherenkov detector	measure neutrino flux precisely & $\nu_e + \text{O CC}^\ddagger$ cross section	2022
LAr TPC	liquid argon time-projection chamber	measure $\nu_e + \text{Ar CC}^\ddagger$ cross section	2025

Current Planned, [‡] charge-current

``CENNS-750" or ``COH-Ar-750" instead of ``COH-Ar-2 ", which may subject to change in the future.

2. Scintillator Detectors

3.1 What is Scintillators?

The incident radiation loses and deposits energy in the scintillator, causing ionization excitation of atoms (or ions, molecules) in the scintillator, and then the excited particles are de-excited to emit scintillation photons with wavelengths close to visible light.

Scintillation materials can be roughly divided into the following three categories: organic scintillators, inorganic scintillators, and organic liquids scintillators.

Organic crystals scintillators are aromatic hydrocarbon compounds containing benzene ring structures interconnected in various ways. Their luminescence typically decays within a few nanoseconds.

Organic liquids scintillators are liquid solutions of one or more organic scintillators in organic solvents. Typical solutes are fluorine. The most widely used solvents are toluene, xylene, benzene, phenylcyclohexane, triethylbenzene and decalin. Liquid scintillators are easily loaded with other additives, such as wavelength shifters to match the spectral sensitivity range of a particular PMT, or ^{10}B to improve the neutron detection efficiency of the scintillation counter itself (because ^{10}B has a high interaction cross section with thermal neutrons).

Plastic scintillator generally refers to a scintillation material in which a primary fluorescent emitter (called a phosphor) is suspended in a substrate of a solid polymer matrix. Although this incorporation is usually achieved by dissolving fluorine prior to bulk polymerization. Advantages of plastic scintillators include fairly high light output and relatively fast signal with decay times of 2-4 nanoseconds.

Inorganic scintillators are usually crystals grown in high temperature furnaces, such as alkali metal halides, and usually contain small amounts of activator impurities. The most widely

used is Na I (Tl) (thallium-doped sodium iodide); its scintillation light is blue. Other inorganic alkali metal halide crystals are Cs I (Tl), Cs I (Na), Cs I (pure). For imaging applications, one of the advantages of inorganic crystals is the very high light yield. My thesis is focusing on the pure CsI crystal.

3.2 Scintillation Mechanism

The scintillation mechanism in CSI depends on the energy states determined by the crystal lattice of materials.

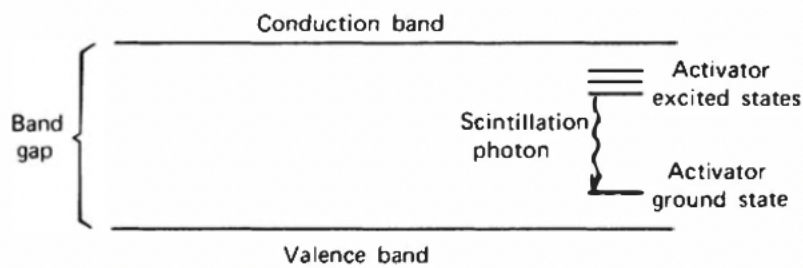


Figure 6 Scintillation Mechanism Principle

In materials classified as insulators or semiconductors, electrons have only discrete energy bands. The lower band, called the valence band, represents those electrons that are essentially bound to lattice sites, while the conduction band represents those electrons that have enough energy to freely migrate throughout the crystal. There is an intermediate energy band, called the forbidden band, where electrons can never be found in pure crystals. The absorption of energy causes an electron to cross the gap from its normal position in the valence band into the conduction band, leaving a hole in the normally filled valence band. In pure crystals, returning electrons to the valence band and emitting photons is an inefficient process. Furthermore, typical

gap widths result in photons with energy too high to be in the visible range.

When activated with thallium, cesium iodide has a very high scintillation light yield. In its pure state, it is also a much weaker scintillator (with output between 5 and 8% of that of NaI(Tl) when measured with a photomultiplier tube). However, much of this light shows a mixture of fast components with an effective decay time of about 10 ns that appears in a peak around 305 nm in the ultraviolet region of the spectrum. A broader emission band in the visible range of 350 to 600 nm that has a much longer decay time of up to several microseconds is also often observed. The relative intensities of these components tend to vary among the measurements reported in the literature for different samples of the material, but they are roughly comparable in yield in one study of commercially supplied crystals. The slow component is absent in other measurements of highly purified material, indicating that its origin may be related to residual impurities in some crystals. In common with pure NaI, unactivated CsI also shows excellent scintillation properties when cooled to liquid nitrogen temperatures. The light yield is about 50,000 photons per MeV, and the decay time is measured to be about 1 microsecond.

3.3 CsI Crystal

Cesium iodide is one of the most widely studied scintillators. Pure CsI crystal is the least hygroscopic. Its emission consists of the fast intrinsic luminescence (10 ns) peaked around 305 nm and a slow component (100-4000ns) around 350-600nm. The fast/slow ratio can reach four when controlled carefully. The total light output is as large as 4-5% of NaI[Tl]. Due to its relatively high density and atomic number, it is one of the brightest scintillators with moderate

gamma ray blocking.

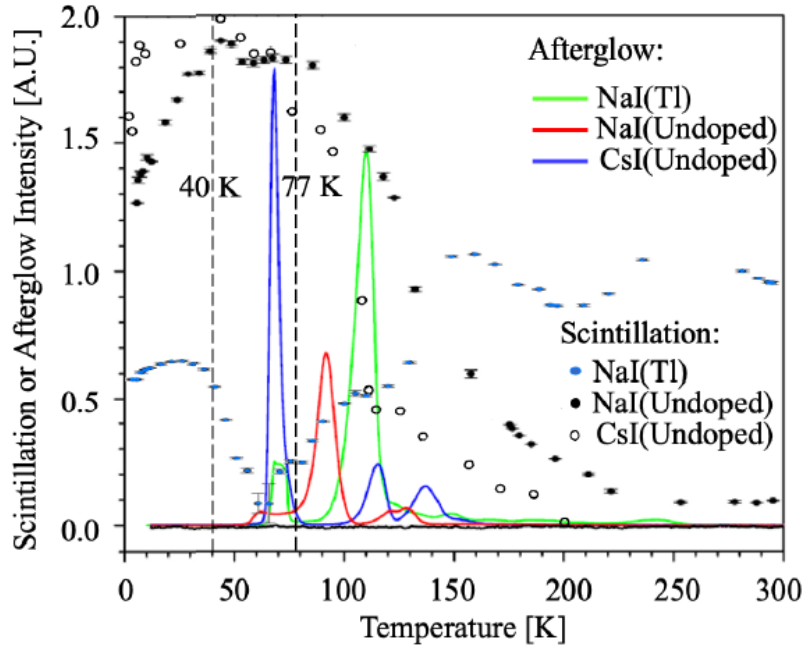


Figure 7 Light yield for different crystal in different temperature

As shown in the Figure 7, the light yield of pure CsI is not higher than other scintillators in room temperature. But it will increase rapidly when temperature goes down. The highest point is around 40K. And we can clearly see that the second peak is around 77K which is the liquid nitrogen (LN₂) temperature. The light yields are twice higher than other CsI[Tl] in room temperature.

3. Light Yield Measurement

3.1 Our cryostat

Previously, we put our cryostat which is filled with N₂ gas to conduct the heat in the LN₂. In this way, it only takes about 30 minutes to cool down the crystal to LN₂ temperature. This cryostat is designed for the quenching factor measurement. The crystal is cooled by the cooling finger. But it will take about 12 hours to cool down the crystal. Because we put the course in the cryostat to measure the light yield. For quenching factor measurement, we need to use neutron beam to do the measurement which is come from the accelerator. In order to avoid the bad influence from LN₂ and N₂ gas. We must cool the crystal by this way.

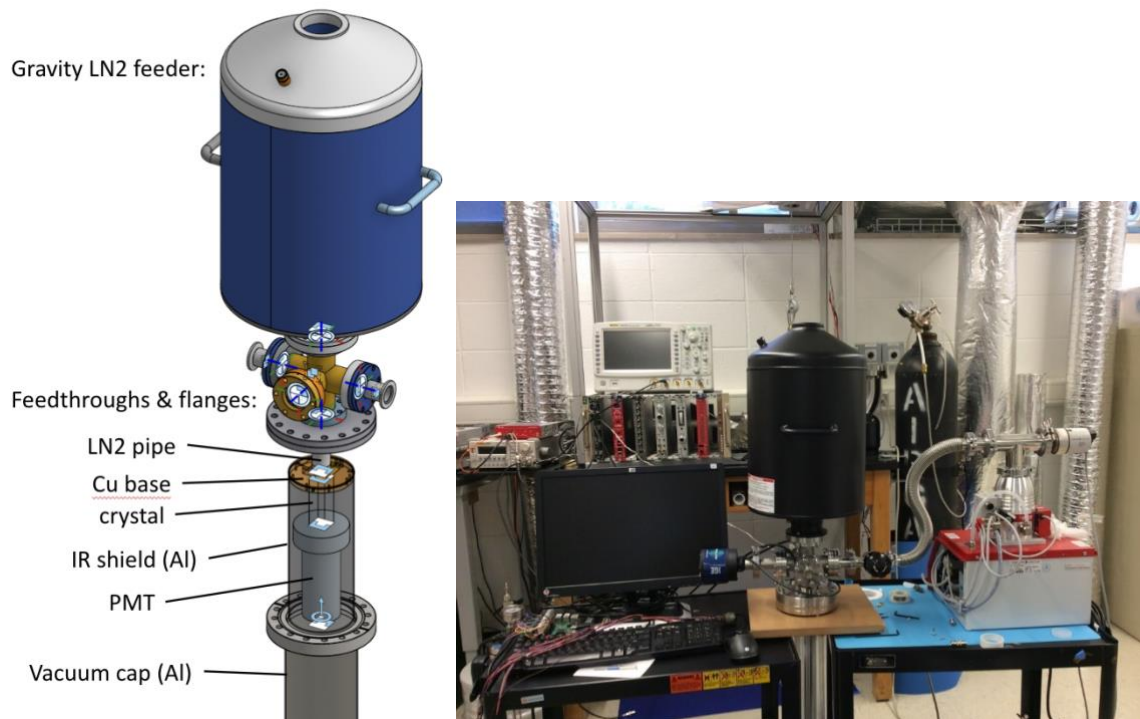


Figure 8 Cryostat design diagram (Left) and the experiment setup in our lab (Right)

We set the LN₂ feeder on top. Due to gravity, liquid nitrogen fills the entire pipe. The pipe goes through the copper base which is fixed on the pipe. We use three stainless steel bars

with springs to push the PMT. And these will also press the crystal against the end of the pipe. This can make sure that the crystal is full contact with the cooling finger. In this way we can be sure that our crystal can reach 77K.

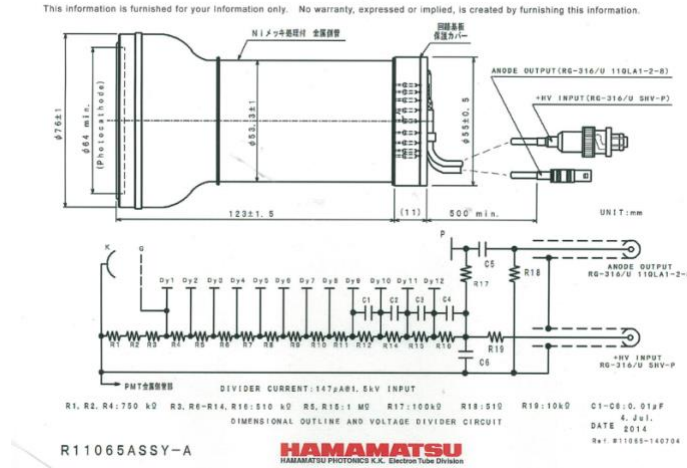


Figure 9 The circuit diagram of PMT

The experimental setup for the measurement is shown in Figure 9. The undoped cuboid crystal was purchased from AMCRYS¹¹, which is 1 inch in diameter and 30 mm in height. All surfaces were mirror polished. To make sure there is no light leak, side surfaces of the crystal were wrapped with multiple layers of Teflon tape. The HAMAMATSU 11065 PMT were used to collect light. A bias voltage of 1500V was applied to the PMT and was kept the same throughout the measurement. Figure 9 shows the circuit diagram of the PMT. The current signal was converted to a voltage one on the 50 Ω internal impedance of the voltage amplifier used in this measurement. To ensure adequate optical contact without optical grease The Figure 10 (left) shows the cryostat and the inside setup. The right figure shows the IR shield.



Figure 10 Cryostat inside setup (left) and the IR Shield (right).

To minimize exposure of the undoped CsI to atmospheric moisture, the assembly was done in a glove bag flushed with dry nitrogen gas. The relative humidity was kept below 5% at 22°C during the assembly process. The crystal assembly was attached to a stainless-steel pipe which is filled with the LN2. the inner diameter of the chamber was 4 inches, and the length is 12 inches. The chamber was vacuum sealed on both ends by two 4-inch ConFlat (CF) flanges. Vacuum welded to the top flange were two BNC, two SHV, one 19-pin electronic feedthroughs. After all cables were fixed inside the chamber, the flange was closed. The chamber was then pumped with a Pfeiffer Vacuum HiCube 80 Eco to 1.2×10^{-4} mbar.

A few Heraeus C220 platinum resistance temperature sensors were used to monitor the cooling process. They were attached to the side surface of the crystal, the top passive board, and the top flange to obtain the temperature profile of the long chamber. A Raspberry Pi 2 computer with custom software was used to read out the sensors. The cooling process took about 20

minutes due to the small size of the crystal. Most measurements, however, were taken after about 40 minutes of waiting to let the system reach thermal equilibrium. The temperature of the crystal was $-195.7 \pm 0.3^{\circ}\text{C}$ during measurements, which was almost the same as the LN_2 temperature.

The passive boards were powered by a RIGOL DP821A DC power supply. A voltage of 1500 V was applied to the PMT. According to their manuals, the voltage can be from 500 V to 2000V. Signals were further amplified by a Phillips Scientific Quad Bipolar Amplifier Model 771, which has four channels, each has a gain of ten. Chaining two channels together, a maximum gain of 100 times can be achieved. A gain of 5 was used. Pulses from the amplifier were then fed into a CAEN DT5720 waveform digitizer, which had a 250 MHz sampling rate, a dynamic range of 2V and a 12-bit resolution. WaveDump, a free software provided by CAEN, was used for data recording. The recorded binary data files were converted to CERN ROOT files for analysis.

3.2 Data format

The digitizer (CAEN DT5751) is used to take the measurement data. All the data is recorded as root file which is a data container called tree.

ROOT is an object-oriented program and library developed by CERN. It was originally designed for particle physics data analysis and contains several functions specific to the field, but it is also used in other applications such as astronomy and data mining. ROOT is a very appropriate tool for use by actuaries and other insurance analysts who do ad hoc data analysis and predictive modeling type work. ROOT is a framework that is specifically designed for large scale data analysis. ROOT stores data in a very efficient way in a hierarchical object-oriented database. This database is machine independent and highly compressed. If one loads a 1 GB text

file into a ROOT file, it will take up much less disk space than the original text file. ROOT also has tools to interact with data in a very efficient way. It has built in tools to do multi-dimensional histograms, curve fitting, modeling and simulation. All these tools are designed to handle large volumes of data. Conversely, relational databases (databases where the data is organized as tables and rows) were originally designed for transactional systems and not for data analysis. Thus a relational database is very good for use in a policy administration system, which looks at one policy at a time, or claim administration system, which looks at one claim at a time. But, when one is interested in segmenting the data across all the policies or across all the claims, a relational solution falls apart. In order to make the relational solution work for large scale data analysis, we use the brute force method. A typical brute force method will involve adding considerable computing power, adding sophisticated I/O capabilities such as cache, etc., adding numerous indices to tables, creating additional summaries of the data (like OLAP cubes), and other similar techniques. If one loads a 1 GB text file into a relational database, it will take up multiple gigabytes to just store the data. When one further tweaks the database for performance with additional indices, pre- summaries and such, the original 1 GB data would have exploded to something very large. Most (if not all) of the commercial software for data analysis is built for accessing data from relational databases. These commercial tools cannot overcome the fundamental flaw in the way data is stored (tables and rows) except by using brute force.

Some data analysis tools are very memory intensive. Some data analysis tools are very I/O intensive. Some data analysis tools are both memory-intensive and I/O-intensive (like most business intelligence tools that run on relational databases). In these systems, the performance of the system degrades exponentially even when the data grows at a linear scale. Therefore, these systems are not easily scalable, and ROOT stores and retrieves data in an optimal way that

facilitates data analysis. It avoids most memory issues and I/O performance issues by buffering data seamlessly between memory and storage. Therefore, even a small PC can get very reasonable throughput from ROOT (all analyses reported in this article were done on PC). A laptop using ROOT as a data analysis tool may be able to provide better performance than a powerful mainframe using one of the commercially available data analysis tools. Therefore, ROOT can be a solution adopted by one person in an insurance company. Once validated, it can be easily scaled to an entire team of data analysts or as an enterprise-wide solution. ROOT solutions are very scalable. ROOT may be a suitable solution even for smaller datasets. Often, predictive modeling and ad hoc data analysis involve presenting data in different graphical/tabular forms. These demos are best done on a laptop device. This is one of the reasons why Excel is so popular among actuaries. Using Excel, people can work with data, and once a story emerges from the data, it can be easily shared with the rest of the team. This concept can be loosely called interactive computing. When you want to analyze a column in an Excel spreadsheet, you must read the entire spreadsheet into memory. Like Excel, other technologies suffer from similar inefficiencies. When data is stored in a relational database in the form of tables and rows, a subset of the data cannot be accessed or modified in an efficient manner without touching the rest of the data. ROOT is designed to allow access to subsets of data without touching the rest. If all the information has to be processed, the entire ROOT file can be read sequentially. In the absence of data explosion issues, the ROOT file can also be randomly read to process only a few attributes if required for analysis. Therefore, ROOT is able to provide us with interactive computing power where other solutions fail. There are many other reasons why ROOT is a suitable tool for predictive modeling. However, the efficiency of storing and accessing data is where ROOT stands out from any other tool on the market today.

3.3 Single PE Measurement

Single PE responses of individual channels were investigated using waveform data triggered by dark counts. Some pre-traces were preserved before the rising edge of a pulse that triggered the digitizer to calculate the averaged baseline value of a waveform, which was then subtracted from each sample of the waveform. Figure 11 shows a typical single PE pulse.

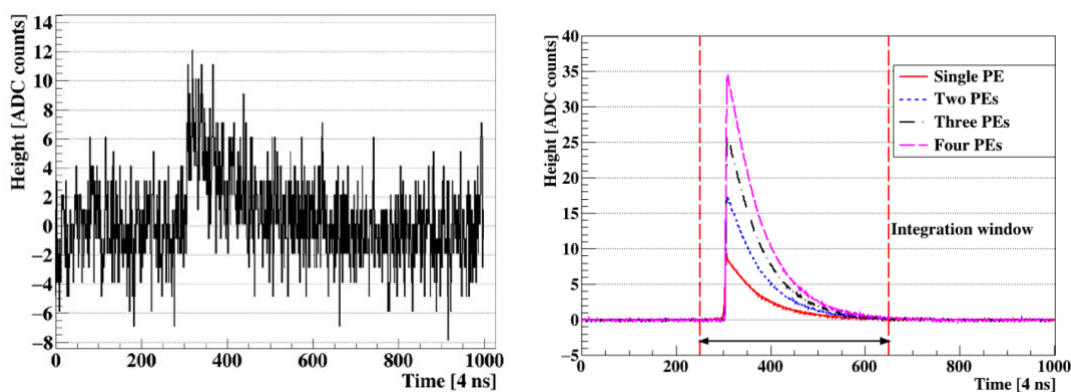


Figure 11 Single PE waveform (left) and the multiple PEs waveform (right)

Overshooting or undershooting after a pulse may be hidden in a noisy baseline, especially for small PE pulses. A common way to remove the effect of electronic noise is to calculate the average waveform corresponding to the same PEs. For example, the average waveform of single PEs. PE was obtained by first adding up all single PE waveforms and then dividing the summed waveform by the total number of single PE events. The same method was used to obtain the average waveforms of higher PEs. They are all shown in Figure 11. No obvious overshooting or undershooting can be seen; and pulses of different PEs are well contained in the integration window.

Figure 12 shows the distribution of pulse areas given by the integration, where individual PEs can be seen clearly. If the mean of the first peak is multiplied by 2, 3, 4, ... the results

roughly match the means of the second, third, fourth, ... peaks. We hence believe that the second peak is the single PE distribution. The peak was fitted using a Gaussian function to obtain its mean value and the result is shown in Figure 12. The same operations were done for all other peaks. The mean of single PE, $\text{mean}_{1\text{PE}}$ is defined as the Gaussian mean in Figure 12 divided by the number of PEs, n . The $\text{mean}_{1\text{PE}}$ for the second peak equals to $51.01 \text{ ADC counts} \cdot \text{ns}$.

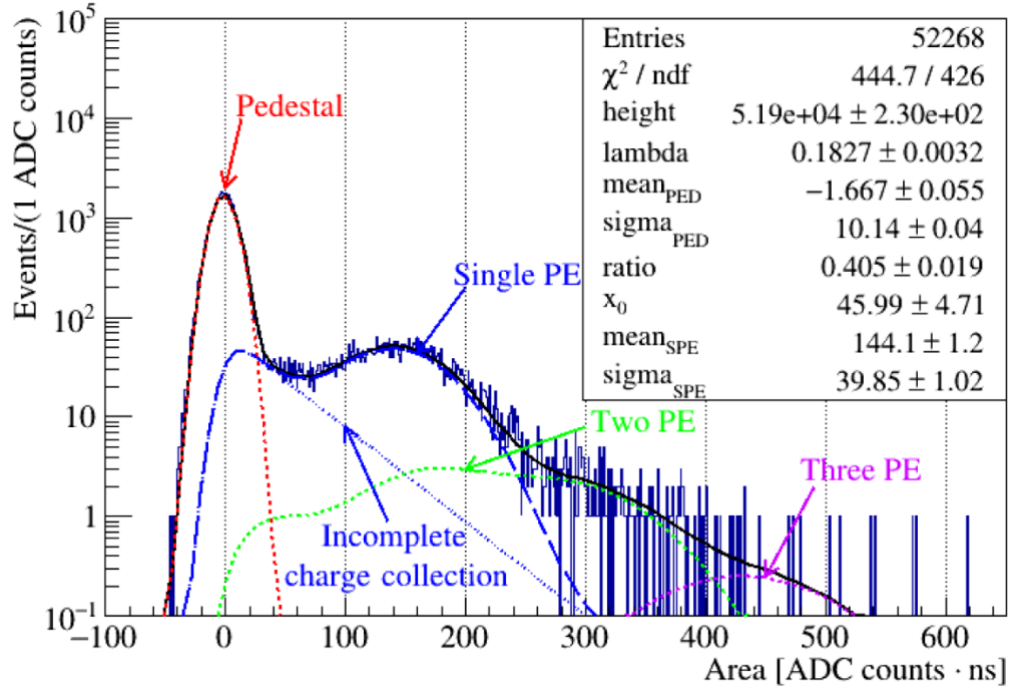


Figure 12 Single PE response fitting from Pedestal to three PEs

The $\text{mean}_{1\text{PE}}$ as a function of the number of PEs is shown in Figure 12. A flat line was expected while a slightly up-going curve was observed from the top PMT. Single PE responses were also measured using an ultraviolet (370~nm) LED from Thorlabs. It was powered by a square pulse that last 20 ns and was emitted at a rate of 10 kHz from an RIGOL DG1022 arbitrary function generator. The voltage of the pulse was tuned to be around 2.78 V so that only zero or one photon hit the PMT under most of the time. Waveforms were recorded whenever a square pulse was generated. They were integrated in a fixed time window.

The energy calibration was performed using X and γ -rays from an Am^{241} and Fe^{55} radioactive source^{15–17}. The source was attached to the vacuum cap. The digitizer was triggered. Pulses induced by radiation from the source were well above the threshold. The integration of a pulse starts 50 samples before the trigger position and ends 10 samples after the position where the pulse goes back to zero. The integration window of a randomly selected light pulse induced by a 59.5 keV γ -rays is shown in Figure 13. The integration has a unit of ADC counts·ns. The recorded energy spectrum in this unit is shown in Figure 13.

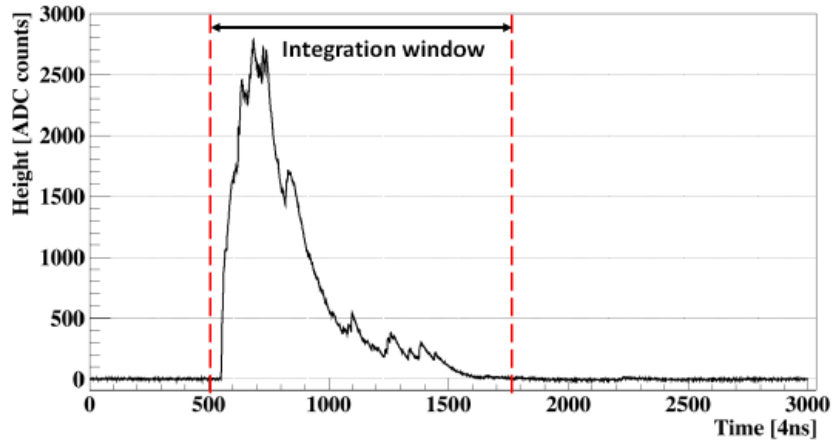


Figure 13 A randomly selected light pulse within the 59.5 keV peak from the PMT.

The origin of each peak was identified and summarized in Table 3. The peak around 200×10^3 ADC counts·ns is a combination of multiple X -rays ranging from 13.8 to 20.1 keV. The averaged mean of these X -rays weighted by their intensities measured in is $17.5 \sim \text{keV}$.

Peaks in Figure 12 were fitted with Gaussian functions to extract their mean values and widths. Most of the right side of the $17.5 \sim \text{keV}$ peak and the left side of the $26.3 \sim \text{keV}$ peak were excluded from the fitting as they overlapped with multiple X -ray peaks around $21 \sim \text{keV}$ in between. The $59.5 \sim \text{keV}$ peak was more or less Gaussian. However, its left side was slightly higher than the right side due to the loss of energy in materials between the source and the

crystal¹⁸.

Table 3 Fitting results of ²⁴¹Am peaks in energy spectra.

Type of radiation	Energy [keV _{ee}]	Mean _{top} [ADC·ns]	Sigma [ADC·ns]	FWHM [%]
X-ray	17.5 [†]	220469	47835.1	51.1
γ-ray	26.3	341799	56719.3	39.1
γ-ray	59.5	730198	57663.1	18.6
Type of radiation	Energy [keV _{ee}]	Mean _{bottom} [ADC·ns]	Sigma [ADC·ns]	FWHM [%]
X-ray	17.5 [†]	268360	56462.2	49.5
γ-ray	26.3	413138	64188.3	36.6
γ-ray	59.5	879406	61193.7	16.4

Table 3 shows the distribution of pulse areas versus pulse heights. A good linearity of the PMT up to 59.5 keV was kept and the pulse height was controlled within the digitizer's dynamic range.

3.4 Light Yield Measurement

The fitted means of the 17.5 keV, 26.3 keV and 59.5 keV peaks in the ²⁴¹Am spectrum in the unit of ADC counts·ns were converted to the number of PE using the formula:

$$(\text{number of PE}) = \frac{(\text{Mean-shift value}) [\text{ADC counts} \cdot \text{ns}]}{\text{mean}_{\text{SPE}}}.$$

The shift value is added to account for the overall shift of the energy spectrum observed in the single PE measurement. However, compared to the mean value, it is much smaller, adding it to the equation does not change the result much.

The light yield was calculated using the data in Table 3 and the following equation:

$$\text{light yield [PE/keV}_{\text{ee}}] = \frac{(\text{number of PE})}{\text{Energy [keV}_{\text{ee}}]}$$

We also use the lower energy source (Fe55) to do the calibration. Because for the quenching factor measurement the energy deposited in the crystal by the neutron is very low. We want to make sure that our threshold is lower than the energy.

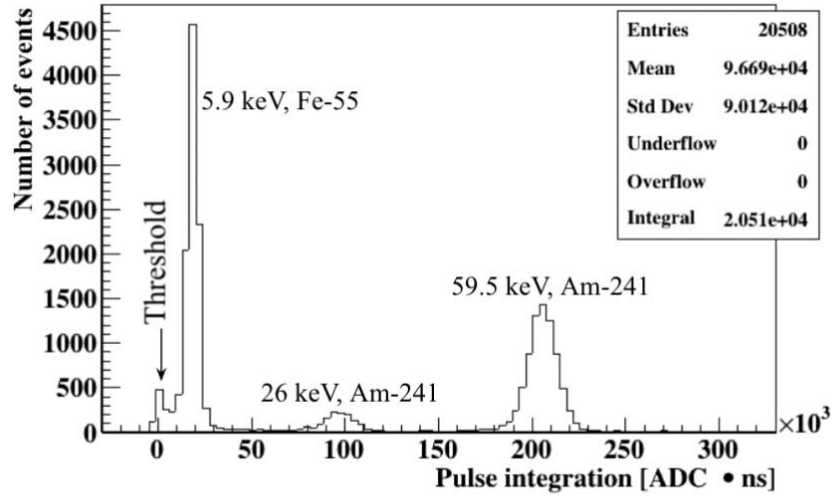


Figure 14 Light Yeld Measurement with Am241 and Fe55 x-axis is the area of the events after intergration

$$\text{light yield} = 210 \times 10^3 \div 59.5 \div 144 = 24.5$$

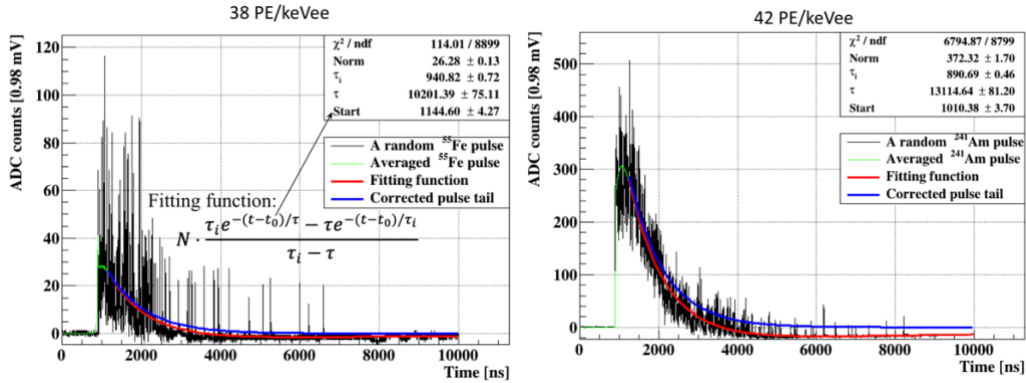


Figure 15 5.9KeV(left) and 59.5KeV(right) overshooting correct

A flat line was fitted to the light yields obtained from the three peaks recorded in PMT. The uncertainties of the light yield measurements are mostly determined by the uncertainties of the $\text{means}_{\text{SPE}}$. The light yield observed by the PMT is $24.5 \text{ PE/keV}_{\text{ee}}$. Based on our limited experience, the influence of self-absorption is not as significant as those of optical surface conditions and light collection efficiencies of light sensors, as we observed larger light yields in larger crystals coupled to PMTs with higher quantum efficiencies and better wrapping of crystals.

Figure 14 shows the light measurement with Am241 and Fe55 inside the crystal. We can clearly distinguish between the Fe55 peak and the baseline. That means that our threshold can be low to 5.9 Kev which the X-ray produced by the Fe55. And we use the Am241 peak to calculate the light yield of our crystal.

We checked the 59.5 Kev waveforms. We can see that the waveform has the overshooting which means the light yield is less the actual value. We use the fitting function to fit the overshoot waveform.

The fitting function:

$$N \frac{\tau_i e^{-(t-t_0)/\tau} - \tau e^{-(t-t_0)/\tau_i}}{\tau_i - \tau}$$

After correcting overshooting, we got $38 \text{ PE/keV}_{\text{ee}}$.

4. Quenching Factor Measurement

4.1 Quenching factor

Quenching factor (QF) is the scintillation light yield from nuclear recoil relative to the scintillation light yield from electron recoil at the same energy. The electron recoil response is usually measured using a gamma ray source, in which case the QF can be expressed as:

$$QF = \frac{E_{meas}}{E_{recoil}} = \frac{L_{meas}E_{\gamma,calib}}{E_{recoil}L_{\gamma,calib}}$$

where E_{recoil} , E_{meas} are the recoil energy of the nucleus produced by WIMP nucleus scattering and the experimentally measured energy by the crystal detector respectively. Since the light output, L_{meas} , is measured in the scintillator, E_{meas} can be obtained from the calibration. $L_{\gamma,calib}$ is the measured scintillation light yield for gamma rays with a known energy E_{γ} .

The quenching factors of CsI crystals used in the KIMS experiment have been previously measured. Subsequently, it has been suggested that channeling effects in the scintillation crystal might enhance the quenching factors to as high as $QF \simeq 1$ for some specific nuclear-recoil conditions. Channeling occurs when a recoil ion in the target material moves in a direction that is within a critical angle from a symmetry axis or plane in the crystal lattice. In these cases, the recoil ion primarily loses energy via numerous scatterings with atomic electrons around target nuclei that are confined to small scattering angles because of the relatively large impact parameters between the moving ion and target nuclei. As a result, channeling effects show up as enhanced ion penetration ranges and larger numbers of electron-hole pairs in the target material with a resultant smaller stopping power. The large penetration range enhances the scintillation effects have only been studied using ions that are incident from outside of the crystal into the empty space between symmetrically aligned lattice atoms. Thus, conclusions from previous

studies of channeling effects might not apply to recoil ions from WIMP-nucleus scattering, which occur inside the crystal. In these cases, recoil ions, originally located at a crystal lattice point, initially travel at a large angle from the adjacent target nuclei located near the symmetry axis or crystal plane because of a small initial impact parameter. As a result, the recoil ions cannot easily channel through the empty space near the symmetric axis; this is known as the blocking effect. Bozorgnia et al. point out that recoiling lattice ions have some chance to be channeled through the symmetric axis due to thermal lattice vibrations. Nevertheless, the fraction of full channeling for isotropically scattered recoil ions is expected to be below 10 % for CsI crystals.

4.2 Simulation

We used Geant4 to finish the simulation. Geant4 (Geometry and Tracking) was developed by the European Nuclear Center (CERN) in 1994. It is a tool that uses C++ as the underlying language and Monte Carlo method to simulate the transportation of particles in materials. It is open to all users. And open source. The main application areas are high energy physics/nuclear physics/accelerator physics/nuclear medicine. Due to the authenticity of its simulation, it can provide users with simulation results that are not much different from the real experimental results, which is convenient for users to evaluate and modify the experiment before the real experiment.

After setting the input items and output items, Geant4 will simulate according to the user's settings. In the case of successful reading and no errors, the particle source in Geant4 will emit a specified particle, which will interact with the material set by the user. The type of interaction/deposition energy/action time and other attributes are determined by Monte Carlo

sampling decides, and the probability of sampling comes from Geant4's own database of particle-material interaction. Some of these databases are the results of experimental measurements and some are the results of theoretical calculations.

The life cycle of a particle from emission to interaction with the material and finally deposited inside the material to enter a stable state or fly out of the geometric range of this simulation is an example, which is called "Event" in Geant4.

The interaction between particles and materials may have multiple trajectories due to the generation of secondary particles. For example, when photons interact with materials, the secondary particles produced include electrons. This electron will continue to interact with the material to create a trajectory. In Geant4, the trajectory of each particle or secondary particle in the material is called "Track".

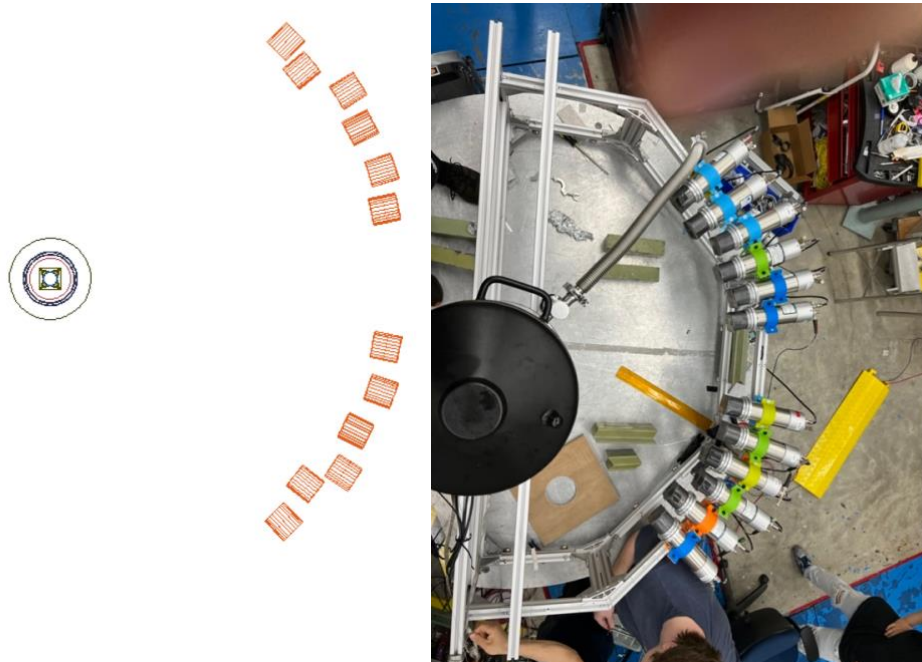


Figure 16 Simulation back detectors setup(left) and back detectors setup(right)

It should be noted that there may be multiple interactions between particles and materials; therefore, Geant4 uses the interaction that occurs on each track as a node, and divides each track into several steps, which are called "Steps" in Geant4. Each Step represents an interaction between the particle and the material. Most of the information in the output item is recorded in the unit of step, and the information recorded is the time/location/deposited energy of this interaction.

The position and the angle have been measured to do the simulation. Figure 16 shows the experiment and the simulation setup. The simulation use the exact same position and angle as our experimental setup. 10 million random neutron beams are used to shoot the crystal.

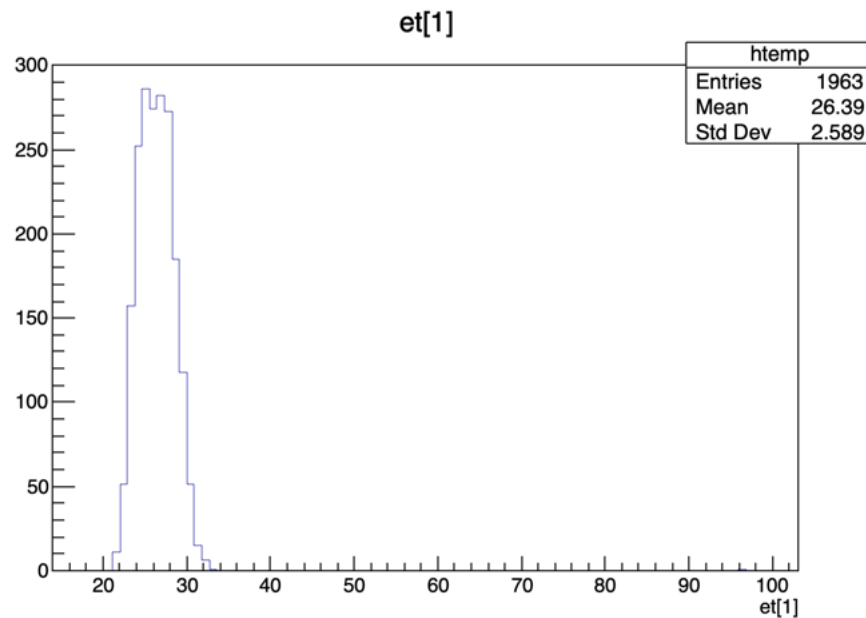


Figure 17 Energy deposit in crystal triggered on 32.3 degree back detector.

Error! Reference source not found. shows the energy deposit in the crystal. The x-axis shows the energy. And the y-axis shows the number of entries. We select the event which has only one hadron elastic in the crystal. We can see the total entries are 1963. The efficiency can

be calculated by $1963/10^8 = 0.2 \pm 0.01\%$. This will help us to determine how long should we use the beam in the future measurement. We can see the value of energy is concentrated at around 25 keV which is higher than our threshold. That means We can clearly distinguish them from the baseline.

4.3 Time of Flight Measurement

In order to check the neutron energy, we measured the speed of neutron. We can simply calculate the speed by

$$Velocity = \frac{Distance}{Time} \quad 4.1$$

We selected three distances (1.66m, 2.36m, and 3.15m) from the beam window. Because we are not sure the distance between the beam starting point and the beam window. So, we set three check points to calculate it.

$$Velocity = \frac{Distance2 - Distance1}{Time2 - Time1} \quad 4.2$$

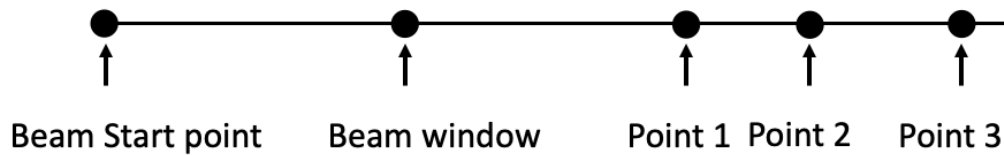


Figure 18 Time of flight measurement setup principle

Neutron beams for these measurements were produced at the tandem van de Graaff accelerator facility of TUNL. Neutrons are produced by accelerating deuteron nuclei hitting deuterium gas. We can control the energy of the neutrons produced by controlling the electric field that accelerates the deuteron.

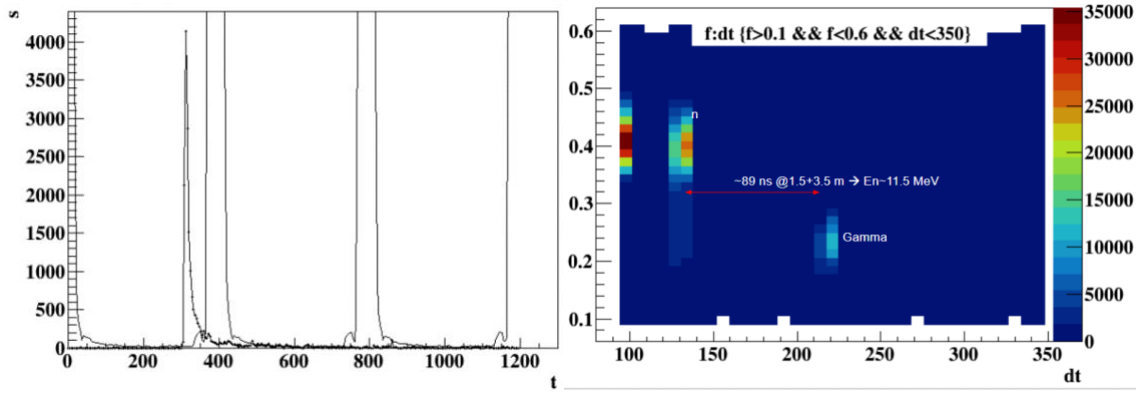


Figure 19 Time of flight of 3.5m neutron events(left) and neutron and gamma events concentration

Figure 19 shows the time of flight at 3.5 m from the beam window. In the left figure, the higher waveform shows the periodic deuteron pulses. The lower waveform shows the neutron pulse. In the right figure, the time difference between neutrons and gamma is 89 ns.

We measured the distance between gas cell and the beam window is 1.5m. And we roughly calculate the energy of the neutron using this distance.

Table 4 Neutron events time of flight at different distance

	Distance(m)	Time difference(ns)
Point 1	1.67	60.6
Point 2	2.36	74.3
Point 3	3.16	89

According to equation 4.2, we can calculate the energy of the neutron beam is 11.5 MeV.

4.4 Light Yield Measurement with PMT

The previous light yield measurement was finished in our lab to test the threshold and the light yield. But in TUNL we used different DAQ to collect the signal. We adjusted the amplifier multiplier from 20 times to 5 times to avoid the saturation.



Figure 20 Experiment Setup (Left figure is the whole experiment setup. The vacuum machine is on the right. The right figure shows the hardwares.)

There will be some changes in light yield and SPE over time, which will cause experimental errors, so we measure it every two hours. Figure 21 shows the change of the light and SPE in every two hours. The light yield stabilizes around 39 PE/KeV. The SPE will vary more. We take their evaluation value calculation to reduce the error.

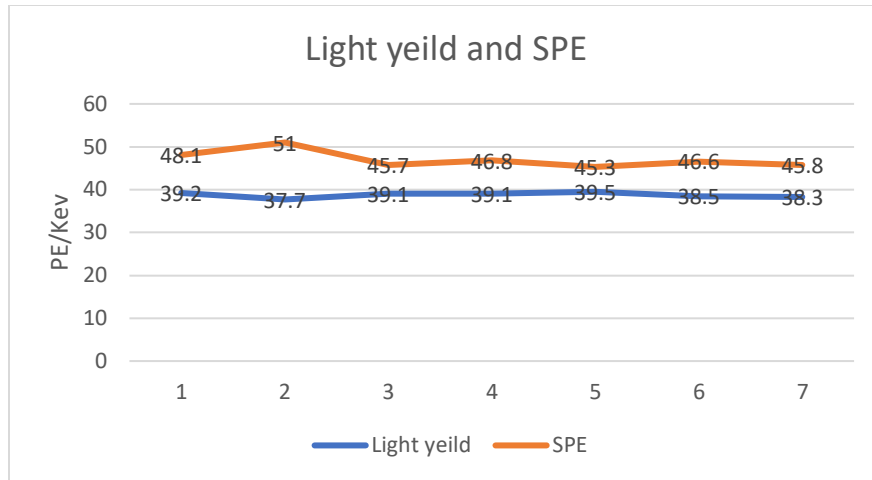


Figure 21 Light yeild(blue) and SPE(orange) measurement over time(every 2 hours during the QF measurement)the unit of x-axis is 2 hours between each other.

4.5 Quenching Factor Measurement

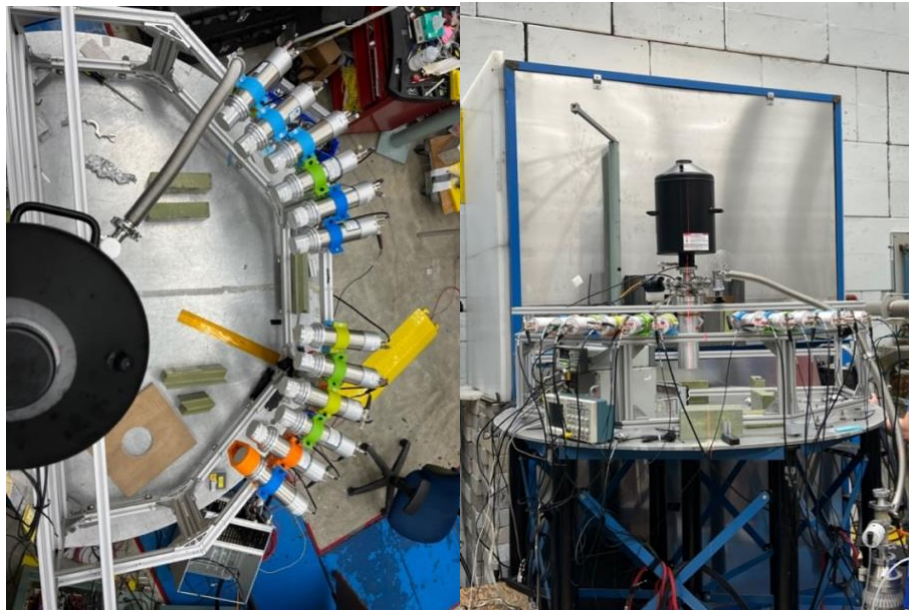


Figure 22 Top view of the experiment setup (left) and Front view of experiment setup (right).

We used the same experimental setup as time-of-flight measurement. But the back detectors are used to collect the neutron and gamma ray. The model of the back detectors is EJ-

309 liquid scintillator detectors. This detector is particularly sensitive to neutrons and photons.

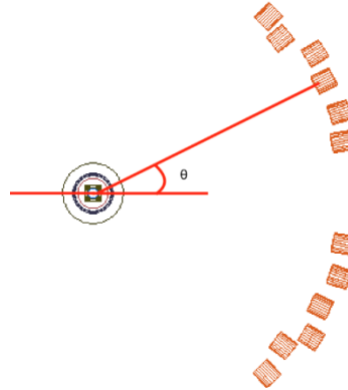


Figure 23 Quenching Factor Measurement principle.

If we can control the energy of the neutrons, we can calculate the energy from the angle. This is the E_{recoil} . Our measurement method is to record the signals of all detectors, especially the CSI detectors, as long as there is a signal in one back detector. So, we get the angle of reflection and the energy deposited in the detector which is E_{meas} .

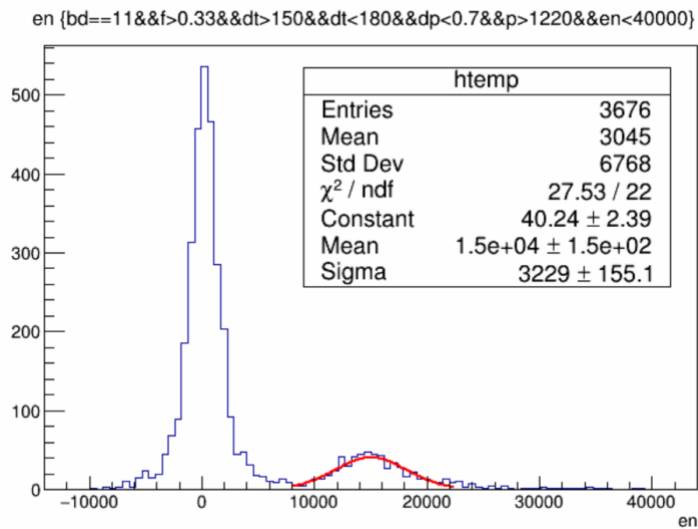


Figure 24 Energy deposit in the crystal triggered on 45 degree back detector

Figure 24 shows the energy statistics of the CSI detector when trigger on 45 degrees back detector. The red Gaussian distribution shows the nucleus recoil energy distribution. The energy is $15000/50/39 = 7.69\text{keV}$.

The quenching factor is $7.69 / 51.7 = 14.88 \pm 0.07\%$.

5. Conclusion

In chapter 3.4, We verified that undoped CSI has good scintillation performance in low temperature environment. This proves that pure CSI really has potential as a detector for detecting low-energy particles. In chapter 4, the result of our quenching factor measurement is acceptable. We choose the largest angle to analysis. The energy of the neutron has more energy than the smaller angle. But when the angle goes small, the concentration of the neutron will merge to the background concentration. At this situation, the data analysis will be more difficult. And at the smaller angle, we need to focus on the effect of background photons on our result. Because the number of photons we can detect is already very low, the effect of background photons will be very serious in this case. So, the rest of our data analysis need to be more careful. We need to reduce the effect of background photons on our experimental results. Overall, our measurement was successful, but we need to spend more time on data analysis. In next step, we need to compare our result with the simulation results to make sure our results are reasonable. This would make our results more convincing.

References

- (1) Barbeau, P. S.; Efremenko, Yu.; Scholberg, K. COHERENT at the Spallation Neutron Source. **2021**.
- (2) Barranco, J.; Miranda, O. G.; Rashba, T. I. Probing New Physics with Coherent Neutrino Scattering off Nuclei. *JHEP* **2005**, *12*, 021. <https://doi.org/10.1088/1126-6708/2005/12/021>.
- (3) Tomalak, O.; Machado, P.; Pandey, V.; Plestid, R. Flavor-Dependent Radiative Corrections in Coherent Elastic Neutrino-Nucleus Scattering. *JHEP* **2021**, *02*, 097. [https://doi.org/10.1007/JHEP02\(2021\)097](https://doi.org/10.1007/JHEP02(2021)097).
- (4) Akimov, D.; others. Simulating the Neutrino Flux from the Spallation Neutron Source for the COHERENT Experiment. **2021**.
- (5) Akimov, D.; others. A D₂O Detector for Flux Normalization of a Pion Decay-at-Rest Neutrino Source. *JINST* **2021**, *16* (08), P08048. <https://doi.org/10.1088/1748-0221/16/08/P08048>.
- (6) Coloma, P.; Esteban, I.; Gonzalez-Garcia, M. C.; Maltoni, M. Improved Global Fit to Non-Standard Neutrino Interactions Using COHERENT Energy and Timing Data. *JHEP* **2020**, *02*, 023. [https://doi.org/10.1007/JHEP02\(2020\)023](https://doi.org/10.1007/JHEP02(2020)023).
- (7) Denton, P. B.; Gehrlein, J.; Pestes, R. \$CP\$ -Violating Neutrino Nonstandard Interactions in Long-Baseline-Accelerator Data. *Phys Rev Lett* **2021**, *126* (5), 051801. <https://doi.org/10.1103/PhysRevLett.126.051801>.
- (8) Coloma, P.; Gonzalez-Garcia, M. C.; Maltoni, M.; Schwetz, T. COHERENT Enlightenment of the Neutrino Dark Side. *Phys Rev D* **2017**, *96* (11), 115007. <https://doi.org/10.1103/PhysRevD.96.115007>.
- (9) Akimov, D.; others. Measurement of the Coherent Elastic Neutrino-Nucleus Scattering Cross Section on CsI by COHERENT. **2021**.
- (10) Collar, J. I. Quenching and Channeling of Nuclear Recoils in NaI(Tl): Implications for Dark-Matter Searches. *Phys. Rev. C* **2013**, *88* (3), 035806. <https://doi.org/10.1103/PhysRevC.88.035806>.
- (11) AMCRYS. <http://www.amcrys.com/>
- (12) MicroFJ-SMTPA-60035. www.mouser.com/datasheet/2/308/1/MICROJ_SERIES_D-1489647.pdf
- (13) Piatek, S. Silicon Photomultiplier Technical Consultant Operation, Performance & Possible Applications.
- (14) Biland, A.; Bretz, T.; Buß, J.; Commichau, V.; Djambazov, L.; Dorner, D.; Einecke, S.; Eisenacher, D.; Freiwald, J.; Grimm, O.; Gunten, H. von; Haller, C.; Hempfling, C.; Hildebrand, D.; Hughes, G.; Horisberger, U.; Knoetig, M. L.; Krähenbühl, T.; Lustermann, W.; Lyard, E.; Mannheim, K.; Meier, K.; Mueller, S.; Neise, D.; Overkemping, A.-K.; Paravac, A.; Pauss, F.; Rhode, W.; Röser, U.; Stucki, J.-P.; Steinbring, T.; Temme, F.; Thaele, J.; Vogler, P.; Walter, R.; Weitzel, Q. Calibration and Performance of the Photon Sensor Response of FACT — the First G-APD Cherenkov Telescope. *J. Instrum.* **2014**, *9* (10), P10012–P10012. <https://doi.org/10.1088/1748-0221/9/10/P10012>.
- (15) Ding, K.; Chernyak, D.; Liu, J. Light Yield of Cold Undoped CsI Crystal down to 13 KeV and the Application of Such Crystals in Neutrino Detection. *Eur Phys J C* **2020**, *80* (12), 1146. <https://doi.org/10.1140/epjc/s10052-020-08712-2>.
- (16) Campbell, J. L.; McGhee, P. L. State-of-the-Art Efficiency Determination for a Si(Li) X-Ray Detector in the 3–40 KeV Energy Range. *Nucl Instrum Meth A* **1986**, *248* (2), 393–

404. [https://doi.org/10.1016/0168-9002\(86\)91024-7](https://doi.org/10.1016/0168-9002(86)91024-7).
- (17) Chu, S. Y. F.; Ekström, L. P.; Firestone, R. B. WWW Table of Radioactive Isotopes.
 - (18) Chernyak, D.; Pershey, D.; Liu, J.; Ding, K.; Saunders, N.; Oli, T. Prospect of Undoped Inorganic Crystals at 77 Kelvin for Low-Mass Dark Matter Search at Spallation Neutron Source. *Eur Phys J C* **2020**, *80*, 547.
 - (19) COHERENT Collaboration; Akimov, D.; others. Observation of Coherent Elastic Neutrino-Nucleus Scattering. *Science* **2017**, eaao0990.
 - (20) Liu, J.; Yamashita, M.; Soma, A. K. Light Yield of an Undoped CsI Crystal Coupled Directly to a Photomultiplier Tube at 77 Kelvin. *JINST* **2016**, *11* (10), P10003. <https://doi.org/10.1088/1748-0221/11/10/P10003>.
 - (21) COSINE-100 Collaboration; Adhikari, G.; others. Search for a Dark Matter-Induced Annual Modulation Signal in NaI(Tl) with the COSINE-100 Experiment. *Phys. Rev. Lett.* **2019**, *123* (3), 031302. <https://doi.org/10.1103/PhysRevLett.123.031302>.
 - (22) Bernabei, R.; others. First Model Independent Results from DAMA/LIBRA-Phase2. *Nucl Phys Energy* **2018**, *19* (4), 307–325. <https://doi.org/10.15407/jnpae2018.04.307>.
 - (23) Amaré, J.; others. First Results on Dark Matter Annual Modulation from the ANAIS-112 Experiment. *Phys Rev Lett* **2019**, *123* (3), 031301.
 - (24) Amaré, J.; others. Performance of ANAIS-112 Experiment after the First Year of Data Taking. *Eur Phys J C* **2019**, *79*. <https://doi.org/10.1140/epjc/s10052-019-6697-4>.